Automated tuning of inter-dot tunnel coupling in double quantum dots

C. J. van Diepen,[1,2,3] P. T. Eendebak,[1,3] B. T. Buijtendorp,[1,2,3] U. Mukhopadhyay,[1,2] T. Fujita,[1,2] C. Reichl,[4] W. Wegscheider,[4] and L. M. K. Vandersypen[1,2]
[1]*QuTech, Delft University of Technology, P.O. Box 5046, 2600 GA Delft, The Netherlands*
[2]*Kavli Institute of Nanoscience, Delft University of Technology, P.O. Box 5046, 2600 GA Delft, The Netherlands*
[3]*Netherlands Organisation for Applied Scientific Research (TNO), P.O. Box 155, 2600 AD Delft, The Netherlands*
[4]*Solid State Physics Laboratory, ETH Zürich, 8093 Zürich, Switzerland*

(Received 27 March 2018; accepted 26 June 2018; published online 16 July 2018)

Semiconductor quantum dot arrays defined electrostatically in a 2D electron gas provide a scalable platform for quantum information processing and quantum simulations. For the operation of quantum dot arrays, appropriate voltages need to be applied to the gate electrodes that define the quantum dot potential landscape. Tuning the gate voltages has proven to be a time-consuming task, because of initial electrostatic disorder and capacitive cross-talk effects. Here, we report on the automated tuning of the inter-dot tunnel coupling in gate-defined semiconductor double quantum dots. The automation of the tuning of the inter-dot tunnel coupling is the next step forward in scalable and efficient control of larger quantum dot arrays. This work greatly reduces the effort of tuning semiconductor quantum dots for quantum information processing and quantum simulation.

https://doi.org/10.1063/1.5031034

Electrostatically defined semiconductor quantum dots are actively studied as a platform for quantum computation[1–3] and quantum simulation.[4,5] Control over the inter-dot tunnel coupling is a key ingredient for both applications. Via control over the tunnel coupling, we have control over the exchange coupling, which is vital for realizing the various proposals for spin-based qubits.[1,6,7] Based on the natural description of semiconductor quantum dots in terms of the Fermi-Hubbard model, control over the tunnel coupling allows for analog simulations to explore the physics of interacting electrons on a lattice.[8,9]

An obstacle for the efficient use of semiconductor quantum dots are the background charged impurities and variations in the gate patterns, which lead to a disordered potential landscape. Initial disorder can be compensated for by applying individually adjusted gate voltages. Additionally, even though gates are designed to specifically control a chemical potential or a tunnel coupling, in practice, capacitive coupling induces cross-talk from all gates to dot chemical potentials and tunnel couplings. The disorder and cross-talk increase the complexity of tuning up ever larger dot arrays. The effort of tuning can be reduced by automation based on image processing. Earlier work on automation of tuning for semiconductor quantum dots has shown that it is possible to automatically form double quantum dots with a sensing dot (SD), and to find the single electron regime in the double dot, however, without the control of the inter-dot tunnel coupling.[10] More recently, such automated tuning routines were used to determine the initialization, read-out, and manipulation points for a singlet-triplet qubit.[11] Machine learning was used for the automated tuning between an open channel, a single dot and a double quantum dot regime in a nanowire.[12] An automated control over the inter-dot tunnel coupling is an important next step forward in control for scaling up the number of spin qubits in semiconductor quantum dots.

In this letter, we present a computer-automated algorithm for the tuning of the inter-dot tunnel coupling in semiconductor quantum dot arrays and demonstrate the algorithm on separate double dots. The algorithm consists of two parts. Part I determines a virtual barrier gate, which corresponds to a linear combination of voltages to apply on multiple gates in order to adjust the tunnel barrier without influencing the chemical potentials in the dots. To determine such a virtual barrier gate, we model and fit the capacitive anti-crossings measured in charge stability diagrams. Part II tunes the tunnel coupling using a feed-back loop, which consists of stepping the virtual barrier gate value and measuring the tunnel coupling, until the tunnel coupling converges to a user-defined target value. To measure the tunnel coupling, we use two methods. The first method is based on photon-assisted tunneling[13] (PAT), while the second method is based on the broadening of the inter-dot transition line.[14] We describe the algorithm and demonstrate its power by automatically tuning the tunnel coupling to a target value for two double dots. We show results for tuning both to higher and lower tunnel couplings for several different initial values, both for a single electron and for two electrons on the double dot.

The platform used for the demonstration of the algorithm is a linear triple quantum dot device.[15] A scanning electron microscopy image of a device similar to the one used in our experiment is shown in Fig. 1(a). By applying voltages on gate electrodes on the surface of a GaAs/AlGaAs heterostructure, we shape the potential landscape in the two-dimensional electron gas 85 nm below the surface. Gates *LS* and *RS* are designed to control the tunnel couplings to the left and right reservoir, respectively. Additionally, plunger

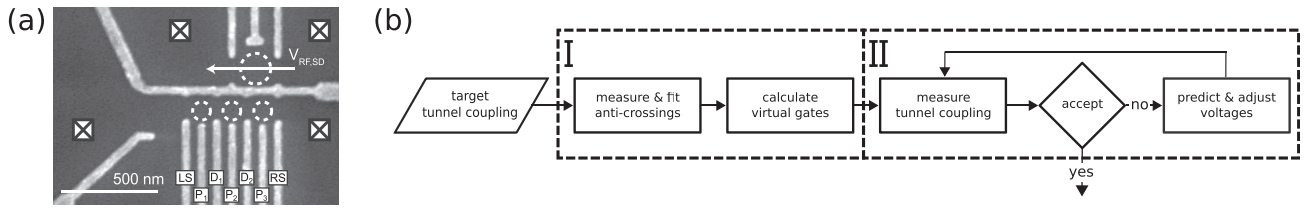

FIG. 1. (a) A scanning electron microscopy image of a device nominally identical to the one used for the measurements. The three smaller dashed circles indicate the positions of the dots in the array. The larger dashed circle indicates the location of the sensing dot. Squares indicate Fermi reservoirs, which are connected to ohmic contacts. (b) A flowchart of the automated tunnel coupling tuning algorithm. The dashed boxes indicate the two parts of the algorithm.

gates, P_i, are designed to control the chemical potential of dot i, and barrier gates, D_i, are designed to control the inter-dot tunnel coupling between dot i and dot $i+1$. The device allows for the formation of three quantum dots in a linear configuration, which are indicated with three white dashed circles in the bottom part of Fig. 1(a). In the present work, we focus on two of the three dots at a time. There is one additional dot, indicated with the larger white dashed circle in the upper part, which we refer to as the sensing dot (SD), because it is operated as a charge sensor, utilizing its capacitive coupling to the three other quantum dots. One of the SD contacts is connected via a bias-tee to a resonator circuit, permitting fast read-out of the charge configuration in the bottom dots, by measuring the SD conductance with radio-frequency reflectometry. To optimize the sensitivity of the charge sensor, we operate the SD half-way on the flank of a Coulomb peak. Automation on the tuning of the sensing dot for read-out was already shown in Ref. 10. One of the bottom gates, P_2, is connected to a microwave source, used for PAT measurements.

As a starting point for our algorithm, we assume that the device is tuned near an inter-dot charge transition. Such a starting point can be obtained from a computer-automated tuning algorithm.[10] We also require a rough estimate of the electron temperature for the modelling of charge transition line widths. For the PAT measurements, we calibrated the microwave power such that we only observe single-photon lines.[13]

Part I of the algorithm [see Fig. 1(b)] determines the virtual plunger and barrier gates by measuring the cross-capacitance matrix (see supplementary material II), which describes the capacitive couplings from gates to dot chemical potentials. To determine this matrix, we measure charge stability diagrams with charge sensing and fit the avoided crossing with a classical model (supplementary material Fig. S1). The fitting of the anti-crossings is based on finding the minimum of the sum over all pixels of the difference between the processed data and a two-dimensional classical model of the avoided crossing (see supplementary material III). From the fit of the anti-crossing, we obtain the slopes of all five transition lines: four addition lines, where an electron moves between a reservoir and a dot, and the inter-dot transition line, where a charge moves from one dot to the other. We fit the anti-crossing to charge stability diagrams measured for any combination of P_i, P_{i+1}, and D_i over a range of 40 mV around the starting point, to fill in the entries of the cross-capacitance matrix. From the inverse of this matrix, we obtain both the virtual barrier, $\tilde{D}_i$, and the virtual plungers, $\tilde{P}_i$ and $\tilde{P}_{i+1}$. The effectiveness of this basis transformation in voltage-space becomes clear from the right angles between addition lines in the charge stability diagram in the 2D-scan of $\tilde{P}_i$ and $\tilde{P}_{i+1}$ in Fig. 2(a). The anti-crossing fit also provides the voltages at the center position on the inter-dot transition line, indicated with the white dot. The white dotted line indicates the detuning axis, which will be used as a scanning axis in the second half of the algorithm.

Before describing part II of the algorithm, let us first explain the two methods we use to measure the tunnel coupling. The first method is PAT [see Figs. 2(b) and 2(e)], which is based on the re-population of states induced by a microwave field. We can observe the re-population using the sensing dot, when the different states correspond to different charge configurations. While varying the frequency of the microwave source, we observe resonance peaks when the frequency is equal to the energy difference between two states. By scanning over the detuning axis and finding the resonance peaks, we perform microwave spectroscopy to map out (part) of the energy level diagram, from which we determine the tunnel coupling. We obtain the tunnel coupling by using a fitting procedure that consists of three steps. First, we process the data per microwave frequency, mainly subtracting a smoothed background signal taken when the microwave source is off. Second, we find the extrema in this processed signal per microwave frequency, and last we fit the curve(s) that connects the extrema using a model of the energy level diagram. For the PAT measurement with a single electron as shown in Fig. 2(b), we model the system in terms of two levels with energies as shown in Fig. 2(c). The resonance curve is then described by $hf = \sqrt{\varepsilon^2 + 4t^2}$, where h is Planck's constant, f the applied microwave frequency, t the inter-dot tunnel coupling, and ε the detuning, which is given by $\alpha(\delta\tilde{P}_i - \delta\tilde{P}_{i+1})$, with α the lever arm, a conversion factor between voltage and energy scales.[13] If two electrons occupy the two tunnel coupled dots at zero magnetic field, there are three relevant energy levels at modest detuning, two corresponding to hybridized singlet states and the other to threefold degenerate triplet states [see Fig. 2(f)].[2,16] This level structure results in three possible transitions, with the corresponding energy differences between the singlet and triplet states described by $hf = \pm\frac{\varepsilon}{2} + \frac{1}{2}\sqrt{\varepsilon^2 + 8t^2}$, indicated with the green and blue wiggly arrows, respectively, and the energy difference between the two singlet states given by $hf = \sqrt{\varepsilon^2 + 8t^2}$, indicated with the red wiggly arrow. In the measurement shown in Fig. 2(e), we only observe two out of the three transitions. This we explain by observing that the thermal occupation of the lowest excited state is negligible. We note that some PAT transitions involve a spin-flip, which is mediated by the spin-orbit interaction and a difference in the Overhauser fields between the two dots.[17] The variation

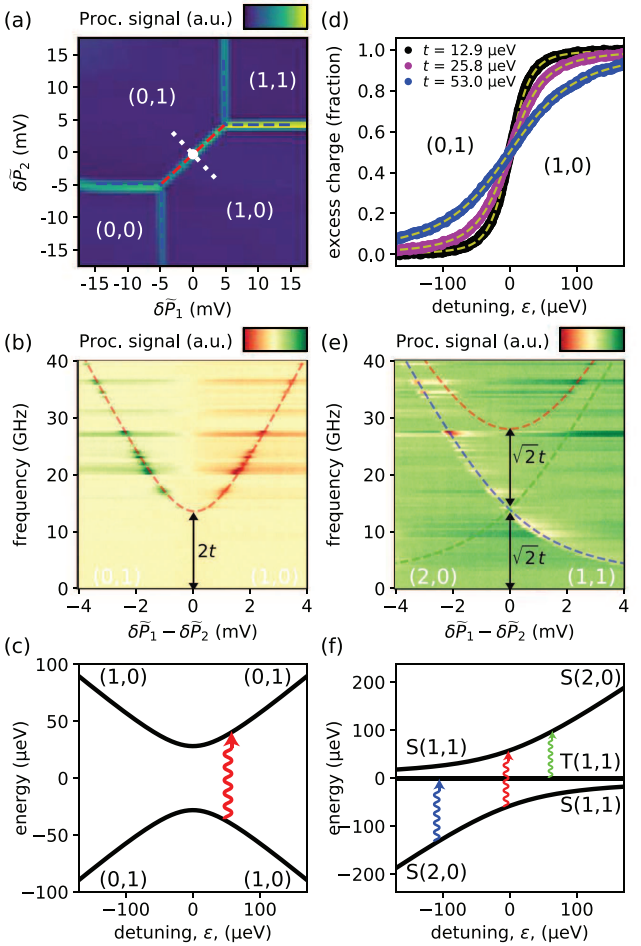

FIG. 2. In all subfigures, (N_1, N_2) indicates charge occupation of the left and middle dot, with no dot formed on the right. (a) A double quantum dot charge stability diagram, showing the processed sensing dot signal as a function of virtual plunger gate voltages. The fitted anti-crossing model is indicated with dashed lines. The detuning axis is indicated with the white dotted line and the center point on the inter-dot transition line with a white dot. (b) Photon-assisted tunneling measurement showing the charge detector signal (background subtracted) as a function of frequency and inter-dot detuning at the (0,1) to (1,0) transition. The red dashed line is a fit of the form $hf = \sqrt{\varepsilon^2 + 4t^2}$. The detuning lever arm is extracted from the slope of the hyperbola in the large detuning limit. (c) The energy level diagram for one-electron occupation. The eigenenergies are $\pm\frac{1}{2}\sqrt{\varepsilon^2 + 4t^2}$. A microwave photon (red wiggly arrow) can induce a transition (and potentially tunnelling between the dots) when the difference between the energy levels corresponds to the photon energy (PAT). (d) Excess charge extracted from a fit to the sensing dot signal as a function of ε for different t, measured by scanning over the detuning axis for the single-electron occupation. The model used to fit to the SD signal is $V(\varepsilon) = V_0 + \delta V Q(\varepsilon) + [\frac{\delta V}{\delta\varepsilon}|_{Q=0} + \left(\frac{\delta V}{\delta\varepsilon}|_{Q=1} - \frac{\delta V}{\delta\varepsilon}|_{Q=0}\right)Q(\varepsilon)]\varepsilon$. Here, V_0 is the background signal, δV is a measure of the charge sensitivity, Q the excess charge as a fraction of the electron charge, and $\frac{\delta V}{\delta\varepsilon}$ the gate-sensor coupling when ε is varied.[9] (e) Photon-assisted tunneling measurement similar to (b) but for the inter-dot transition from (2,0) to (1,1). Coloured dashed lines are fits to the measured data. (f) The energy level diagram for the two electron transition. Coloured wiggly arrows indicate microwave photon excitations. The energy levels are given by $\frac{\varepsilon}{2} \pm \frac{1}{2}\sqrt{\varepsilon^2 + 8t^2}$ for the singlets and are 0 for the degenerate triplets.

in intensity for different horizontal lines in Figs. 2(b) and 2(e) is caused by the frequency dependence of the transmission of the high-frequency wiring. One could compensate for this by adjusting the output power of the microwave source per frequency. The blue tails in Fig. 2(e) are caused by sweeping gate voltages at a rate which is of the same order of magnitude as the triplet-singlet relaxation rate. This was confirmed by inverting the sweep direction and observing that the blue tails appear on the other side of the transition line.

The second method to measure the tunnel coupling is based on the broadening of the inter-dot transition line[14] [see Fig. 2(d)]. The broadening reflects a smoothly varying charge distribution when scanning along the detuning axis, caused by the tunnel coupling via the hybridization of the relevant states and the temperature through the thermal occupation of excited states. For the single-electron case, the average excess charge on the left (right) dot is given as

$$Q = \frac{1}{\mathcal{Z}}\sum_n (c_n e^{-E_n/k_B T_e}), \tag{1}$$

with $\mathcal{Z}$ the partition function, $c_n = \frac{1}{2} \mp \varepsilon/E_n$ the probability of finding the excess charge on the left (right) dot for the eigenstate with energy E_n, and the thermal energy $k_B T_e \approx 10.5$ μeV, with T_e the effective electron temperature. An analogous expression applies to the two-electron case, with $c_n = 0$ for the triplets and $c_n = \frac{1}{2}\left(1 \pm \varepsilon/\sqrt{\varepsilon^2 + 8t^2}\right)$ for the hybridized singlets. The lever arm used for measuring the tunnel coupling from the broadening of the inter-dot transition line is obtained from PAT, but could also be measured with Coulomb diamonds or bias triangles.[2] Based on Eq. (1), we obtain the model for the charge sensor response when scanning over the detuning axis (see the caption of Fig. 2).[9]

Here, we compare the two methods for extracting the tunnel coupling. An advantage of the method based on the broadening of the inter-dot transition line is that it is about two orders of magnitude faster than PAT (see Table I in the supplementary material), because it is effectively a single scan over the detuning axis while PAT is a series of scans over the detuning axis for different microwave frequencies. Another difference is in the range of tunnel couplings over which the two methods work well. For PAT, the upper limit depends on the maximum frequency that the microwave source can produce. We expect that the lower limit for PAT is determined by charge noise, resulting in broadening of the PAT peaks. With PAT, we were able to automatically measure tunnel coupling values as low as 5 μeV. The lower limit for the inter-dot transition broadening method is set by the effective electron temperature, $k_B T_e$, here ≈ 10.5 μeV.[14] The upper limit for this method is that for very large tunnel couplings, the broadening of the inter-dot transition line extends to the boundaries of the charge stability region. In the measurements shown here, we did not come close to this upper limit, but tunnel couplings up to 75 GHz ≈ 300 μeV have been measured with the inter-dot transition line broadening method.[9] We observe that the two methods are in good correspondence with one another, i.e., the difference between the two is smaller than 10% of their average value (see supplementary material V). Measurement errors are usually smaller than the accuracy in target tunnel coupling we are interested in, while potential outliers will typically be caused by unpredictable charge jumps.

Now, let us describe part II of the algorithm [see Fig. 1(b)] which performs a feedback loop. For each iteration, the virtual barrier gate value, i.e., the linear combination of gate

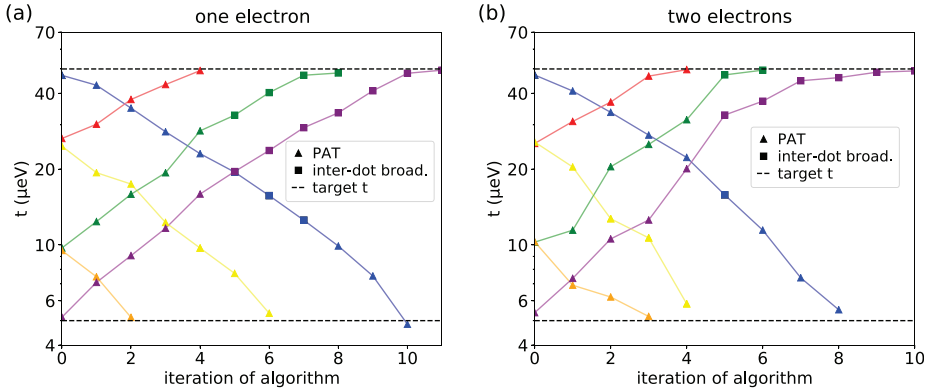

FIG. 3. Results of the algorithm for a transition involving (a) single-electron states and (b) two-electron states. Each panel shows results for different runs of the algorithm indicated by different colors. Triangles indicate tunnel coupling values measured with PAT and squares indicate measurements based on inter-dot transition line broadening. Solid lines are added as a guide to the eye. The black dashed lines indicate the high and low target tunnel coupling values.

voltages as determined in part I, is adjusted and the tunnel coupling is measured. Before the first step of the algorithm, we measure the tunnel coupling with PAT. For this initial measurement, we cannot rely on the (faster) method based on the broadening of the inter-dot transition, since at this stage, the lever arm has not yet been determined. If we are not yet within 1 μeV, of the user-defined target tunnel coupling value, we step the virtual barrier gate value with the step size equal to the maximal step size in the positive direction if the tunnel coupling is too low and vice versa. We limit the barrier gate step size to 20 mV such that the position of the anti-crossing can again be located automatically by fitting the anti-crossing model. For larger step sizes, the position of the anti-crossing becomes harder to predict due to non-linearities. After stepping the virtual barrier gate, we measure the tunnel coupling again using PAT. Then, we have measured the tunnel coupling for two settings and we determine the next step for the virtual barrier, by predicting the voltage required to reach the target value from an exponential fit[9,18] to the measured tunnel couplings and their respective virtual barrier values (we thereby force the exponential to go to zero for very negative barrier voltages). After the tunnel coupling has been measured five times with PAT, we also have five measured lever arm values for different gate voltages. The small differences in lever arm we interpret as caused by small shifts in the dot positions with the gate voltages. We predict the lever arm for other voltages using a linear approximation (see supplementary material V). Using this knowledge of the lever arm, the algorithm can be sped up for the subsequent iterations by measuring the tunnel coupling from inter-dot transition broadening.

Following the procedure described earlier, the algorithm automatically tunes the inter-dot tunnel coupling to a target value, within the range of the measurable tunnel coupling values and the achievable values with our gate design and electron occupations. Figure 3 shows the results of the tuning algorithm for various initial and target tunnel coupling values, indicated with different colours. The target tunnel coupling values are indicated with black dashed lines. We clearly see that the algorithm finds the gate voltages that bring the tunnel coupling to the target value, stepwise moving closer. In Fig. 3(a), the results for the left pair of dots with a single electron are shown, while Fig. 3(b) shows the results for an occupation with two electrons. We have obtained similar results for the second pair of neighbouring dots in the triple dot (see supplementary material VII). The duration of a run of the algorithm mainly depends on the difference between the initial and the final tunnel coupling value, because we limit the maximum step size. The time the tuning algorithm takes to tune an inter-dot tunnel coupling is on the order of 10 min (see supplementary material VI for more details).

In conclusion, we have shown automation of the tuning of the tunnel coupling between adjacent semiconductor quantum dots. Key for this automation was image processing methods to automatically fit the shape of an anti-crossing and to find the shape of the resonance curve in a PAT measurement. The present methods for measuring inter-dot tunnel couplings and the feedback routine can be extended to larger quantum dot arrays, in the future including also two-dimensional arrays. When tuning multiple tunnel couplings, cross-talk effects from the tuning of one tunnel coupling on the values of nearby tunnel couplings will have to be compensated for, which so far was done by hand.[9] This work demonstrates further automated control over semiconductor quantum dots and is the next step forward in automated tuning of larger quantum dot arrays, necessary for scaling up the number of spin-based qubits implemented with semiconductor quantum dots.

See supplementary material for the explanation of the concept of virtual gates, details on the fitting routines, comparison between the two methods to measure the tunnel coupling, data on the automated tuning of another double dot, and information about the time required for the tuning algorithm.

The authors acknowledge useful discussions with T. Hensgens, J. P. Dehollain, and other members of the Vandersypen group, experimental assistance by C. A. Volk and A. M. J. Zwerver, and technical support by M. Ammerlaan, J. Haanstra, S. Visser, and R. Roeleveld. This work was supported by the Netherlands Organization for Scientific Research (NWO Vici), and the Dutch Ministry of Economic Affairs through the allowance for Top Consortia for Knowledge and Innovation (TKI) and the Swiss National Science Foundation.

[1]D. Loss and D. P. Divincenzo, Phys. Rev. A **57**, 120 (1998).
[2]R. Hanson, L. P. Kouwenhoven, J. R. Petta, S. Tarucha, and L. M. K. Vandersypen, Rev. Mod. Phys. **79**, 1217 (2007).
[3]F. A. Zwanenburg, A. S. Dzurak, A. Morello, M. Y. Simmons, L. C. Hollenberg, G. Klimeck, S. Rogge, S. N. Coppersmith, and M. A. Eriksson, Rev. Mod. Phys. **85**, 961 (2013).

[4]T. Byrnes, N. Y. Kim, K. Kusudo, and Y. Yamamoto, Phys. Rev. B **78**, 075320 (2008).
[5]P. Barthelemy and L. M. K. Vandersypen, Ann. Phys. (Berl.) **525**, 808 (2013).
[6]J. Levy, Phys. Rev. Lett. **89**, 147902 (2002).
[7]D. P. DiVincenzo, D. Bacon, J. Kempe, G. Burkard, and K. B. Whaley, Nature **408**, 339 (2000).
[8]S. Yang, X. Wang, and S. Das Sarma, Phys. Rev. B **83**, 161301(R) (2011).
[9]T. Hensgens, T. Fujita, L. Janssen, X. Li, C. J. Van Diepen, C. Reichl, W. Wegscheider, S. Das Sarma, and L. M. K. Vandersypen, Nature **548**, 70 (2017).
[10]T. A. Baart, P. T. Eendebak, C. Reichl, W. Wegscheider, and L. M. K. Vandersypen, Appl. Phys. Lett. **108**, 213104 (2016).
[11]T. Botzem, M. D. Shulman, S. Foletti, S. P. Harvey, O. E. Dial, P. Bethke, P. Cerfontaine, R. P. G. McNeil, D. Mahalu, V. Umansky, A. Ludwig, A. Wieck, D. Schuh, D. Bougeard, A. Yacoby, and H. Bluhm, preprint arXiv:1801.03755 (2018).
[12]S. S. Kalantre, J. P. Zwolak, S. Ragole, X. Wu, N. M. Zimmerman, M. D. Stewart, and J. M. Taylor, preprint arXiv:1712.04914 (2017).
[13]T. H. Oosterkamp, T. Fujisawa, W. G. V. D. Wiel, K. Ishibashi, R. V. Hijman, S. Tarucha, and L. P. Kouwenhoven, Nature **395**, 873 (1998).
[14]L. DiCarlo, H. J. Lynch, A. C. Johnson, L. I. Childress, K. Crockett, C. M. Marcus, M. P. Hanson, and A. C. Gossard, Phys. Rev. Lett. **92**, 226801 (2004).
[15]T. A. Baart, M. Shafiei, T. Fujita, C. Reichl, W. Wegscheider, and L. M. K. Vandersypen, Nat. Nanotechnol. **11**, 330 (2016).
[16]J. R. Petta, A. C. Johnson, J. M. Taylor, E. A. Laird, A. Yacoby, M. D. Lukin, C. M. Marcus, M. P. Hanson, and A. C. Gossard, Science **309**, 2180 (2005).
[17]L. R. Schreiber, F. R. Braakman, T. Meunier, V. Calado, J. Danon, J. M. Taylor, W. Wegscheider, L. M. K. Vandersypen, M. Ni, and M. Pb, Nat. Commun. **2**, 556 (2011).
[18]C. B. Simmons, M. Thalakulam, B. M. Rosemeyer, B. J. Van Bael, E. K. Sackmann, D. E. Savage, M. G. Lagally, R. Joynt, M. Friesen, S. N. Coppersmith, and M. A. Eriksson, Nano Lett. **9**, 3234 (2009).